Applied Catalysis B: Environmental 253 (2019) 170–178

Contents lists available at ScienceDirect

Applied Catalysis B: Environmental

journal homepage: www.elsevier.com/locate/apcatb

Tuning electron density of metal nickel by support defects in Ni/ZrO_2 for selective hydrogenation of fatty acids to alkanes and alcohols

Jun Ni[a,*], Wenhua Leng[a], Jun Mao[a,1], Jianguo Wang[a], Jianyi Lin[b], Dahao Jiang[a,*], Xiaonian Li[a,*]

[a] Institute of Industrial Catalysis, Zhejiang University of Technology, Hangzhou, 310014, China

[b] Energy Research Institute @NTU, Nanyang Technological University, 1 Cleantech Loop, #06-04, CleanTech One, Singapore

ARTICLE INFO

Keywords:
Electron density
Support defect
Nickel catalysts
Selective hydrogenation
Fatty acids

ABSTRACT

Catalysts with tunable activity and selectivity to targeted products are highly demanded when using complex biomass-based resources for the production of fuels and chemicals. Here we synthesize a series of Ni/ZrO_2 catalysts, denoted as iwi-Ni/m-ZrO_2, pc-Ni/t-ZrO_2 and pfc-Ni/t-ZrO_2, prepared by incipient-wetness impregnation (iwi), positive co-precipitation (pc) and parallel flow co-precipitation (pfc) methods, respectively, with the purpose to tune the electron density of nickel in the Ni/ZrO_2 catalysts for the selective hydrogenation of fatty acids to fuel-like alkanes or fatty alcohols. The structural and electronic properties of the catalysts are systematically investigated by N_2 adsorption, XRD, H_2-TPR, H_2-TPD, HRTEM, XPS, in situ FTIR, and DFT calculations. The catalytic performance shows that monoclinic ZrO_2 supported nickel catalysts (iwi-Ni/m-ZrO_2) exhibit the highest selectivity to 1-octadecanol but the lowest selectivity to n-heptadecane, while tetragonal ZrO_2 supported nickel catalysts (pc-Ni/t-ZrO_2 and pfc-Ni/t-ZrO_2), especially the latter possess the highest selectivity to n-heptadecane with the lowest selectivity to 1-octadecanol. This variation in the selectivity is found correlated with the oxygen deficiency of ZrO_2 support which affects the electron density of supported Ni metals. Charge transfer from the support to metal occurs on all the three catalysts, which stems from the electrons trapped in the oxygen vacancies after removing the interfacial O atom in the process of reduction of the ZrO_2 support. The negatively charged metal Ni promotes the heterolysis of hydrogen and the subsequent hydrogenation of adsorbed fatty acids to aldehyde intermediate. Ni metals of much higher excess electron density on m-ZrO_2 (due to its higher reducibility) further catalyze the hydrogenation of the C = O bond of aldehyde to 1-octadecanol while Ni metals with approximate excess electron density on t-ZrO_2 preferentially catalyze the cleavage of the C − CHO bond to produce n-heptadecane.

1. Introduction

The limited availability, supply reliance and related environmental concerns of fossil feedstocks for the production of fuels and chemicals give an impetus to the use of biomass-based resources. Natural fats and oils, which consist of triglycerides and fatty acids, can be converted to renewable and carbon-neutral fuel-like alkanes that are entirely fungible with fossil fuels, or fatty alcohols that are high value-added chemicals. For the production of alkane-based biofuels, a number of catalytic hydrodeoxygenation (HDO) processes have been established over conventional NiMo and CoMo sulfide catalysts [1,2], or noble metals catalysts such as Pt, Pd and Rh [3]. However, the risk of sulfur leaching or the high cost of noble metals render them less environmentally and economically attractive. Hence the hydrotreatment of natural fats and oils by using sulfur-free, non-noble metal-based catalysts, especially Ni-based catalysts has attracted extensive attention recently [4–10]. When Ni catalysts supported on zeolites, Al_2O_3 and SiO_2 were used in HDO of stearic acid (model compound of fats and oils) [11–13], the prevailing products were alkanes whereas a small amount of fatty alcohols could be also detected as an intermediate and disappeared at complete conversion. It is interesting to note that Ni/ZrO_2 catalysts displayed considerable selectivity (33%) towards fatty alcohols even at high conversion (96%) [4]. Although a reaction mechanism for the HDO of fatty acids over Ni/ZrO_2 catalysts was proposed [4,5], in which ZrO_2 provided surface oxygen vacancy sites for the adsorption of fatty acid, the origin of the high selectivity towards fatty alcohols relative to other materials supported Ni catalysts was not elucidated. It inspired us that Ni-based catalysts may have a potential to replace commercial Cu-Cr-

* Corresponding authors.
E-mail addresses: junni@zjut.edu.cn (J. Ni), dhjiang@zjut.edu.cn (D. Jiang), xnli@zjut.edu.cn (X. Li).

[1] Present address: State Key Laboratory of Physical Chemistry of Solid Surfaces, Collaborative Innovation Center of Chemistry for Energy Materials (iChEM), College of Chemistry and Chemical Engineering, Xiamen University, Xiamen, 361005, China.

https://doi.org/10.1016/j.apcatb.2019.04.043
Received 16 November 2018; Received in revised form 10 March 2019; Accepted 15 April 2019
Available online 15 April 2019
0926-3373/

based catalysts for the production of fatty alcohols from natural fats and oils, which will also reduce environmental risks given the use of Cr.

As we know, the catalytic performance of active metal sites on a support is highly influenced by their electronic states. Metal sites can be charged either positively or negatively, depending on the interaction between the active metal and the support. Taking metal oxide (MO) supported Ni catalysts as an example, when Ni interacts with the support via Ni−O−M bond, electron may transfer from Ni to the support through the Ni−O−M bonding and Ni metals become positively charged [14]. When Ni is anchored at oxygen vacancies on the surface, the electrons trapped at the defect sites render the metals negatively charged [15,16]. Positively charged Ni metals are favorable for H_2 evolution, but not for dissociative chemisorption, the latter of which requires d-electron back-donation from Ni to antibonding orbital of H_2 for H_2 activation. Thus, negatively charged metals are preferred in hydrogen involved reactions. For instance, charge transfer from the support to active metals was observed on Ru/TiO_2 catalysts, where electron-donating ability of Ru to adsorbed CO species was enhanced, resulting in an increased stability of adsorbed CO species on Ru nanoparticles and activity for CO methanation [17]. The hydrogenation of carbon dioxide to methanol on Cu/ZnO also benefited from the electron transfer at the Schottky-Mott junction between electron-rich ZnO and Cu, leading to electron-rich active Cu sites [18,19]. For the same reaction on Ga_2O_3-supported Pd catalysts, the Pd metal supported on electron rich plate-shaped Ga_2O_3 showed a better performance than Pd on rod-shaped Ga_2O_3 facets because of more efficient electron transfer [20]. DFT calculations revealed that cation and anion arrangements over the exposed Ga_2O_3(002) surface were unbalanced that they gave an overall non-zero polarity in top layers [21,22]. The coloumbic repulsion between its terminal oxygen anions gave rise to a higher surface energy than other exposed surfaces. As a result, plate Ga_2O_3 had a narrower band gap and their electrons could be promoted easily to conduction band from localized oxygen anions, which would facilitate the oxygen release to create anion vacancies. These excited electrons trapped in oxygen vacancies then transferred to Pd at interface as a way of stabilization of the catalyst [20]. It is thus conclusive that easing the interfacial charge transfer between the two components of a catalyst would likely increase both the reaction rate and selectivity in hydrogenation reactions.

Zirconia as a reducible metal oxide may contain a significant concentration of oxygen vacancies which trap negative electrons at its center [23,24]. ZrO_2 has three common phases. The monoclinic phase (m-phase) with its dominant face (111) is the most stable at low temperatures (< 1000 °C), whereas tetragonal phase (t-phase) with its dominant face (101) and cubic phases (c-phase) are more stable at high temperatures. However doping of a few percentage of low valence cation (Y, Sc, Ca, Mg or Ni) may stabilize t- and c-phases at room temperature. The transition of tetragonal phase with eight-coordinated Zr ion centers to seven-coordinated monoclinic phase is largely dependent on the defect degree of the crystallographic lattice and the presence of additives [25]. These provide a simple way to control the electron density on ZrO_2 surfaces by varying the defect concentration. Thus, we proposed that through selective deposition of metal catalysts on either m-ZrO_2 or t-ZrO_2, one could tune the electronic state of loaded metals and consequently control their catalytic performance.

In this paper, three Ni/ZrO_2 catalysts, denoted as iwi-Ni/m-ZrO_2, pc-Ni/t-ZrO_2 and pfc-Ni/t-ZrO_2, were prepared by incipient-wetness impregnation (iwi), positive co-precipitation (addition of alkaline solution into mixed salts, pc) and parallel flow co-precipitation (simultaneous addition of both alkaline and mixed salt solution, pfc) methods, respectively. The co-precipitation method may facilitate the formation of Ni/Zr oxide solid solution, in which the smaller ionic size (0.076 nm of Ni^{2+} vs. 0.082 nm of Zr^{4+}) and lower ionic charge of Ni^{2+} can lead to the stabilized t-phase with more symmetrical structure and less number of oxygen vacancies than the m-phase [26,27]. As a result the co-precipitation prepared Ni catalysts (pc-Ni/t-ZrO_2 and pfc-Ni/t-ZrO_2) were more positively charged (vs. impregnation prepared catalysts) and exhibited high selectivity to n-heptadecane, while the iwi-Ni/m-ZrO_2 catalyst displayed high selectivity towards 1-octadecanol. The electronic effect induced by support defects of ZrO_2 on the selective hydrogenation of stearic acid to various products was revealed by means of N_2 adsorption, H_2-TPR, H_2-TPD, XRD, HRTEM, in situ FTIR, XPS and DFT calculations. To the best of our knowledge, this is the first demonstration of selective hydrogenation of C_{18} fatty acid to C_{17} alkane or C_{18} alcohol via tuning the electronic structure of active sites, which will also provide a new experimental and theoretical basis for other reactions involving selective hydrogenation of acids.

2. Experimental

2.1. Catalyst preparation

The iwi-Ni/m-ZrO_2 was prepared by an incipient-wetness impregnation method as follows: First, m-ZrO_2 was synthesized by dissolving 0.48 g $ZrOCl_2·8H_2O$ and 9 g urea in deionized water (150 ml) under magnetic stirring. After stirring for 0.5 h, the above aqueous solution was transferred into a Teflon-lined autoclave (250 ml), and then sealed and hydrothermally treated at 453 K for 6 h. The obtained suspension was separated by filtration, washed with deionized water several times, and then dried at 383 K overnight, followed by calcinating in air at 673 K for 4 h in a muffle furnace. The m-ZrO_2 support was then impregnated with appropriate amount of aqueous solution of Ni $(NO_3)_2·6H_2O$. Excess water was removed at 313 K on a rotary evaporator until dryness. The impregnates were dried at 383 K for 4 h and subsequently calcined in air at 773 K for 4 h.

The pc-Ni/t-ZrO_2 catalyst was prepared by a positive co-precipitation method as follows: 17 ml aqueous solution of $Ni(NO_3)_2·6H_2O$ (1 M) and 80 ml aqueous solution of $Zr(NO_3)_4·5H_2O$ (1 M) were premixed. NaOH/Na_2CO_3 solution (1 M) was continuously added into the mixed solution under vigorous stirring till the pH of the mixture was up to 10.7. After precipitation the precipitates were aged for 60 min at room temperature in the mother liquor under continuous stirring.

The pfc-Ni/t-ZrO_2 was prepared by a parallel flow co-precipitation method as follows: 17 ml aqueous solution of $Ni(NO_3)_2·6H_2O$ (1 M) and 80 ml aqueous solution of $Zr(NO_3)_4·5H_2O$ (1 M) were premixed. The mixed solution was added at a constant rate to a stirred tank reactor filled with 100 ml deionized water at room temperature under vigorous stirring. Simultaneously NaOH/Na_2CO_3 solution (1 M) was added to maintain the pH at a constant level of 10.7. After precipitation the precipitates were also aged for 60 min at room temperature in the mother liquor under continuous stirring. All the prepared precipitates derived from above preparation procedures were washed after filtering four times each with deionized water. Finally, the precipitates were dried at 383 K for 10 h and calcined at 773 K for 4 h. Nominal Ni loadings for iwi-Ni/m-ZrO_2, pc-Ni/t-ZrO_2 and pfc-Ni/t-ZrO_2 catalysts were 2 wt.%, 10 wt.% and 10 wt.%, respectively, so that similar particle diameters of Ni nanoparticles could be obtained.

2.2. Catalyst characterization

BET surface areas of the samples were determined by N_2 adsorption using a Quantachrome NOVA 1000e apparatus with liquid-N_2 at the temperature of 77 K. The samples were outgassed at 473 K for 4 h prior to analysis.

H_2-TPR (Temperature-programmed reduction), Adsorption and TPD (Temperature-programmed desorption) experiments were performed on a Micromeritics AutoChem II 2920 apparatus. For H_2-TPR analysis, hundred milligrams of the catalyst sample was placed in a quartz reactor and reduced by a 10% H_2-Ar gas mixture in a flow rate of 50 ml/min with temperature ramping at 10 K/min until 773 K and maintained at 773 K for another 30 min. For H_2-Adsorption and TPD experiments the catalyst sample was pre-reduced for 1 h in a flow of H_2 at 773 K,

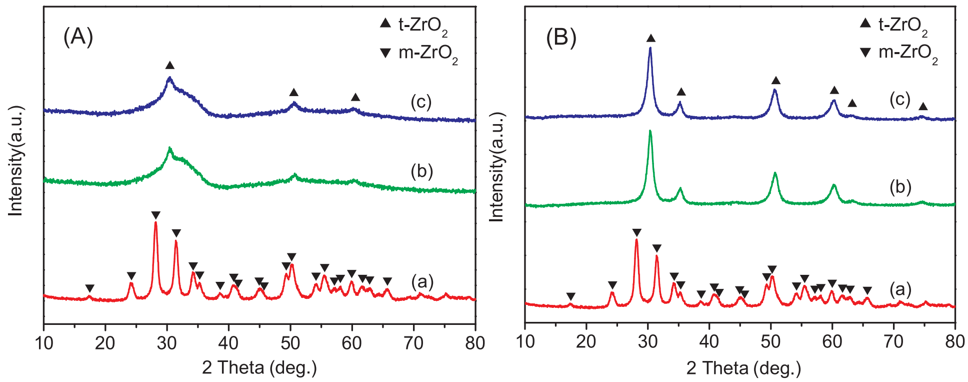

Fig. 1. XRD patterns of the (A) calcined and (B) reduced Ni/ZrO_2 catalysts: (a) iwi-$Ni/m-ZrO_2$; (b) pc-$Ni/t-ZrO_2$; (c) pfc-$Ni/t-ZrO_2$.

purged by Ar at the same temperature for 0.5 h, and then cooled down to 323 K. The H_2 uptake of the reduced catalyst could be determined by pulse-injecting of 10% H_2-Ar till saturation. After the H_2 adsorption testing, the catalyst bed was purged again by He for 30 min at 323 K; then temperature was linearly increased from 323 K to 1073 K at 10 K/min. The active nickel surface area was calculated by the consumption amounts of H_2, assuming that the stoichiometric ratio of $H_{adsorbed}/Ni_{surface} = 1$ and a site density of $6.77 \times 10^{-2}\ nm^2$/atom based on an equal distribution of the three lowest index planes of nickel (fcc) [28]. The Ni dispersion was calculated from H_2 uptake according to the equation:

$$\%D = 1.17X/Wf \quad (1)$$

where X = H_2 uptake in micromoles per gram of catalyst, W = weight percentage of nickel, and f = fraction of nickel reduced to the metal [28,29].

In situ FTIR (Fourier transform infrared spectroscopy) spectra of CO adsorption and desorption were obtained on a Thermo Nicolet 4700 Nexus FTIR spectrophotometer with MCT detector and a quartz reaction cell with BaF_2 windows. The catalyst sample was pre-reduced for 2 h in a flow of H_2 at 773 K, followed by He purging for 30 min. When the sample was cooled to 323 K in He flow, an FTIR spectrum (denoted as background spectrum) was recorded. Pure CO was introduced into the reactor for adsorption. The process of CO adsorption and subsequent desorption by purging with He was continuously recorded. The spectra displayed in the text were obtained by subtracting the background spectrum from the adsorption spectra. All the spectra were recorded with 16 scans with a resolution of 4 cm^{-1}.

XRD (Powder X-ray diffraction) data were collected on an X'Pert PRO X-ray diffractometer between $2\theta = 10°$ and 80° at 2° min^{-1} employing a Cu-Kα radiation source (λ = 0.15406 nm). HRTEM (High-resolution TEM) images were obtained using a Tecnai G2 F30 microscope operated at 200 kV. Before the measurements, the samples were either calcined in air at 773 K for 4 h (for XRD) or pre-reduced in H_2 at 773 K for 2 h (for XRD and HRTEM).

XPS (X-ray photoelectron spectroscopy) spectra were obtained with an ESCALab220i-XL electron spectrometer from VG Scientific using 300 W $Al_{K\alpha}$ radiation and deconvoluted using XPS PEAK41 software. All samples were pre-reduced in a tubular furnace at 773 K for 2 h in a flow of H_2 and transferred under Ar protection into the XPS chamber. The binding energies (BE) were referenced to the graphitic C 1s peak at 284.6 eV, providing accuracy within ± 0.2 eV. The % Lorentzian-Gaussian (L/G) which indicated the fitting degree of peaks was fixed to 20% during deconvolution. The content of each element and its chemical state were calculated based on the areas obtained from the deconvolution results.

2.3. DFT calculations

The DFT calculations were carried out with Vienna Ab-initio Simulation Package (VASP) [30–33]. The inert core electrons were treated with the projector-augmented wave (PAW) [34] pseudo potential and the valance electrons were treated with a plane-wave basis set with cutoff energy fixed at 500 eV. During the structure optimization, the exchange-correlation energy was calculated with exchange-correlation functional proposed by Perdew and Wang [33,34] using generalized gradient approximation. The force criterion of convergence was 10^{-2} eV $Å^{-1}$ on each ion and total energy change criterion of convergence was 10^{-4} eV. The adsorption energy (E_{ad}) of the Ni cluster on ZrO_2 surface was calculated as follows:

$$E_{ad} = E(Ni/ZrO_2) - E(Ni) - E(ZrO_2) \quad (2)$$

2.4. Catalytic reaction

The tests of Ni/ZrO_2 catalysts for hydrogenation of stearic acid were performed using a tank reactor (300 ml capacity) with continuous stirring. Typically, stearic acid (1.0 g) diluted with n-heptane (100 ml) was charged into the vessel, together with Ni/ZrO_2 catalyst pre-reduced at 773 K for 4 h. Before the reaction, the reactor was purged three times with H_2 to exchange the air inside. The reaction was performed at 513 K and 4.0 MPa H_2 (initial pressure at RT) with a stirring rate of 1000 rpm. The products in the gas phase were analyzed by GC–MS with a TCD and an HP-PLOT/Q column (30 m, 0.32 mm inner diameter). The liquid products were analyzed by GC–MS with a flame ionization detector (FID) and a HP-5 column (30 m, 0.25 mm inner diameter). N-tetradecane was used as the internal standard for the quantification of the liquid products.

3. Results and discussion

3.1. Physicochemical properties of the Ni/ZrO_2 catalysts

XRD patterns of three calcined Ni/ZrO_2 catalysts are shown in Fig. 1(A). The intensive diffraction peaks at $2\theta = 24.1°$, 28.2°, 31.5°, 34.1°, 35.3°, 49.3° and 50.1° of monoclinic ZrO_2 crystal phase (JCPDS 01-088-2390, m-ZrO_2) are observed for the calcined iwi-$Ni/m-ZrO_2$ [see Fig. 1(A) a]. For the pc-$Ni/t-ZrO_2$ or pfc-$Ni/t-ZrO_2$ samples [Fig. 1(A) b and c] diffraction peaks at $2\theta = 30.3°$, 35.2°, 50.4°, 50.6° and 60.1° are characteristic of tetragonal ZrO_2 crystal phase (JCPDS 01-080-2155, t-ZrO_2), though they are rather broad and relatively weak. There are no characteristic peaks of NiO for all catalysts as shown in Fig. 1(A). Note that m-ZrO_2 is thermodynamically stable at room temperature while t-ZrO_2 occurs usually at high temperatures [35,36]. A phase transform from monoclinic phase into tetragonal phase is liable to occur [37–39], usually in the presence of additives such Y_2O_3, Sr_2O_3

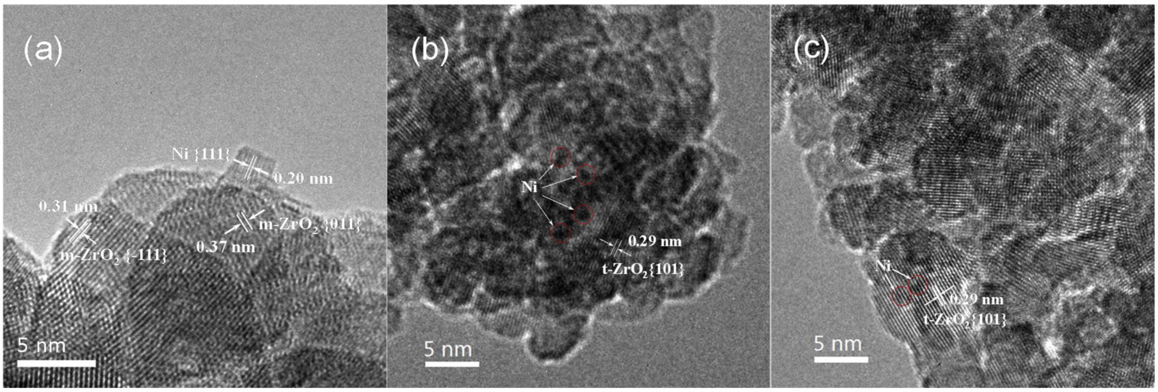

Fig. 2. HRTEM photographs of the reduced Ni/ZrO_2 catalysts: (a) iwi-Ni/m-ZrO_2; (b) pc-Ni/t-ZrO_2; (c) pfc-Ni/t-ZrO_2.

and MgO [25]. Therefore the absence of NiO phase and the existence of t-ZrO_2 in pc-Ni/t-ZrO_2 and pfc-Ni/t-ZrO_2 samples may imply that NiO species are highly dispersive in the calcined Ni/ZrO_2 samples prepared by co-precipitation. Ni^{2+} ions in the crystallographic lattice of ZrO_2 can promote the transition from monoclinic phase into tetragonal phase and stabilize the t-ZrO_2 crystal phase at room temperature.

Fig. 1(B) displays the XRD patterns of the reduced samples. For the reduced iwi-Ni/m-ZrO_2 sample in Fig. 1(B) a, the characteristic peaks of m-ZrO_2 remain sharp and strong. The reduced pc-Ni/t-ZrO_2 and pfc-Ni/t-ZrO_2 samples [Fig. 1(B) b and c] exhibit distinct and intensive characteristic peaks of t-ZrO_2, which may imply that the reduction treatment under H_2 promotes the stabilization of tetragonal phase. Over all samples no crystalline NiO nor Ni phase can be observed. The absence of crystalline Ni peaks appears to indicate high dispersion of reduced Ni metal in the three samples.

HRTEM photographs of the reduced Ni/ZrO_2 catalysts are presented in Fig. 2. For all the Ni/ZrO_2 catalysts, both crystalline size of ZrO_2 nanoparticles and average particle diameter of Ni nanoparticles are comparable (Table 1). The crystalline size of m-ZrO_2 nanoparticles for the iwi-Ni/m-ZrO_2 ranges from 8 nm to 20 nm, while that of t-ZrO_2 nanoparticles for the pc-Ni/t-ZrO_2 and pfc-Ni/t-ZrO_2 ranges from 5 nm to 10 nm. Furthermore, the average particle diameter of Ni nanoparticles on the iwi-Ni/m-ZrO_2 catalyst is around 2.5 nm, while that of Ni nanoparticles on the pc-Ni/t-ZrO_2 and pfc-Ni/t-ZrO_2 is 1.8 and 1.9 nm, respectively. Active Ni surface area of the pc-Ni/t-ZrO_2 or pfc-Ni/t-ZrO_2 catalyst is ca. 2.7 times larger than that of iwi-Ni/m-ZrO_2 due to their higher Ni dispersion and loading (10% vs 2%). The high Ni dispersion in the co-precipitated samples is likely attributed to the strong interaction between NiO and ZrO_2 as demonstrated in the TPR studies (Fig. S1).

H_2-TPD profiles of the three reduced Ni/ZrO_2 catalysts are presented in Fig. 3. The broad H_2 desorption peak at 383 K is observable for all three samples, which is attributed to desorption of H_2 adsorbed on the metal Ni. Though the temperature of the peak is almost the same for three reduced catalysts, the areas of the peak in Fig. 3b and c, i.e. the amount of H_2 desorbed from the Ni active sites on the pc-Ni/t-ZrO_2 and pfc-Ni/t-ZrO_2 catalysts are 7.5 and 7.8 times, respectively, that of the iwi-Ni/m-ZrO_2 catalyst. In Fig. 3a, a weak H_2 desorption peak at ca. 887 K is observable for iwi-Ni/m-ZrO_2. This peak can be attributed to the adsorbed H anions ($H^{\delta-}$) held at coordinatively unsaturated (cus-)

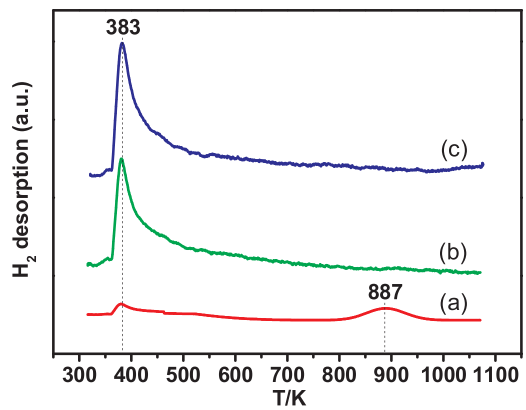

Fig. 3. H_2-TPD profiles of the reduced catalysts: (a) iwi-Ni/m-ZrO_2; (b) pc-Ni/t-ZrO_2; (c) pfc-Ni/t-ZrO_2.

Zr^{3+} ions on the surface of the m-ZrO_2 support [40,41]. It is generally accepted that reducible oxide supports like TiO_2 and ZrO_2 can be partially reduced by hydrogen in the presence of deposited metal particles [42]. Hydrogen which is dissociatively adsorbed on the metal particle may spillover to the ZrO_2 support, reacting with Zr−OH and forming water that then desorbs from the surface with the formation of oxygen vacancies. It is well known that these defects are negatively charged with electron density maximum localized at the center of the oxygen vacancy [23]. Thus the obvious presence of $H^{\delta-}$ on the iwi-Ni/m-ZrO_2 catalyst, which is indistinguishable on the reduced pc-Ni/t-ZrO_2 and pfc-Ni/t-ZrO_2 sample in Fig. 3b and c, implies that oxygen vacancies on the m-ZrO_2 hold more negative charge than those on the t-ZrO_2, in good agreement with the literature [38]. Meanwhile, anionic vacancies also change the oxidation state of the ion from Zr^{4+} to Zr^{3+}, as seen in XPS and FTIR experiments below. These coordinatively unsaturated Zr^{3+} ions stabilize the negatively charged $H^{\delta-}$ for subsequent hydrogenation reactions [40].

XPS Ni 2p, Zr 3d and O 1 s spectra of the reduced Ni/ZrO_2 samples are shown in Fig. 4a–c, respectively. The Ni $2p_{3/2}$ main peak is located at 851.6 eV for iwi-Ni/m-ZrO_2 but shifts to higher BE values at 852.1 and 852.2 eV for pc-Ni/t-ZrO_2 and pfc-Ni/t-ZrO_2, respectively. Moreover the high intensity at ∼854 eV with strong shake-up satellite

Table 1
Textural properties of the Ni/ZrO_2 catalysts.

Catalyst	S_{BET} ($m^2\,g^{-1}$)	Pore volume ($cm^3\,g^{-1}$)	Average pore diameter (nm)	Ni reducibility (%)	Ni surface area (m^2/g_{cat})	Ni dispersion (%)	Ni diameter (nm)	ZrO_2size (nm)
iwi-Ni/m-ZrO_2	73.0	0.46	16.6	0.89	1.9	19.4	2.5	8-20
pc-Ni/t-ZrO_2	123.7	0.19	4.8	0.59	5.6	28.5	1.8	5-10
pfc-Ni/t-ZrO_2	124.5	0.17	4.2	0.55	5.1	28.1	1.9	5-10

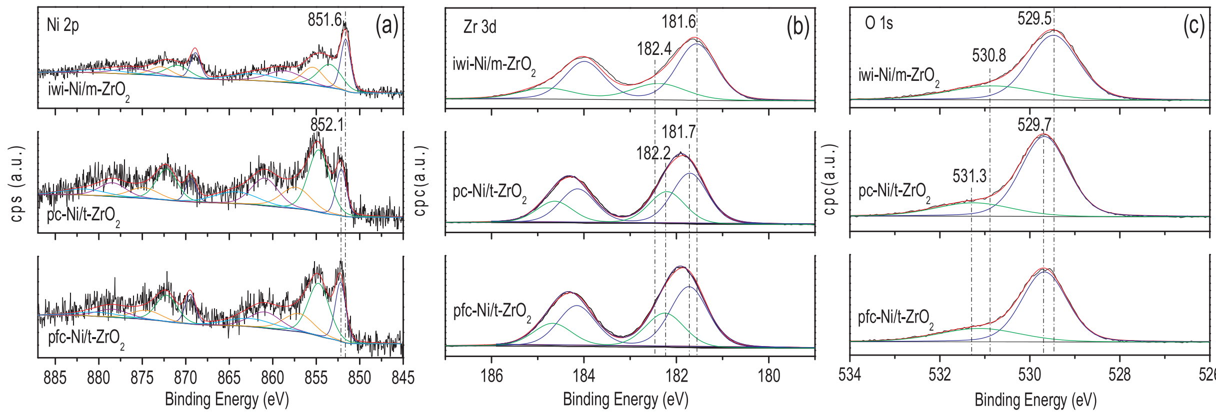

Fig. 4. XPS of Ni 2p (a), Zr 3d (b) and O 1 s (c) core electron level for reduced Ni/ZrO_2 samples.

indicates the existence of Ni^{2+} in the pc-Ni/t-ZrO_2 and pfc-Ni/t-ZrO_2 samples, which corresponds to highly dispersed NiO that stabilizes the t-phase of ZrO_2. Note that all the Ni 2p BE values of the three Ni/ZrO_2 catalysts are evidently lower than that of bulk metal Ni (852.7 eV), indicating the electron-enrichment of our ZrO_2-supported Ni metal. The enrichment of negative charge on the Ni nanoparticles is associated with the electron accumulation at the metal/oxide interface accompanied by O vacancies formation during partial reduction of ZrO_2 support. The electron density of metal Ni on the iwi-Ni/m-ZrO_2 sample is higher than that on pc- or pfc-Ni/t-ZrO_2 due to higher defect charge density of m-ZrO_2 support. This situation is similar to the study of morphology effect over Cu/ZrO_2 by Rhodes and Bell [38] who ascribed the higher CO adsorption capacity of Cu/m-ZrO_2 to the higher concentration of surface anionic vacancies of the m-ZrO_2.

The Zr 3d core level of iwi-Ni/m-ZrO_2 in Fig. 4b can be decomposed into two pairs of spin-orbit-splitting peaks, corresponding to two kinds of zirconium species, referred as species I with Zr $3d_{5/2}$ at 181.6 eV (Zr_I) and species II at 182.4 eV (Zr_{II}), respectively. The lower binding energy Zr_I is attributed to an oxygen-deficient phase of zirconia with partially reduced Zr species (Zr^{3+}); while the higher binding energy signal is attributed to stoichiometric ZrO_2 (Zr^{4+}) [24,43–45]. The fraction of Zr_I species for the iwi-Ni/m-ZrO_2 sample is much larger compared to those for the pc-Ni/t-ZrO_2 or pfc-Ni/t-ZrO_2 sample, which implies the presence of more oxygen-deficient zirconia phase in the iwi-Ni/m-ZrO_2 sample. The binding energy of Zr_I species for the iwi-Ni/m-ZrO_2 sample is also lower than those for the pc-Ni/t-ZrO_2 or pfc-Ni/t-ZrO_2 sample, indicating the higher electron density of Zr_I species due to the higher concentration of anionic vacancies on the surface of iwi-Ni/m-ZrO_2.

The XPS O 1 s spectra of the reduced Ni/ZrO_2 samples in Fig. 4c can be deconvoluted into two peaks. According to the literature [24,41], they can be assigned to the lattice oxygen in the reduced Ni/ZrO_2 samples (O_I) at 529.5 eV and the oxygen species of Zr−OH or Ni−O (O_{II}) at 530.8–531.3 eV, respectively, the latter of which is much lower in intensity. The atomic ratio of O_I/Zr, which can be used to evaluate the concentration of oxygen vacancies on the surface, increases in the order of iwi-Ni/m-ZrO_2 (2.34) < pc-Ni/t-ZrO_2 (2.41) < pfc-Ni/t-ZrO_2 (2.51), suggesting that the ability to form oxygen vacancies on the surface follows the order: iwi-Ni/m-ZrO_2 > pc-Ni/t-ZrO_2 > pfc-Ni/t-ZrO_2, which is in line with the variation of electron density of metal Ni.

We then further used CO as a probe to study the electronic state of Ni and the presence of Zr species on the reduced Ni/ZrO_2 catalysts by in situ FTIR. As shown in Fig. 5a, CO adsorption bands at 2080, 2057, 2014, 1975 and 1912 cm^{-1} are detected on the iwi-Ni/m-ZrO_2 sample soon after the CO exposure. They are ascribed to the linear and bridge-bonded CO on metallic Ni respectively [46–48]. With increasing the CO doses, the IR bands at 2126 and 2185 cm^{-1} start to grow and overlap with gas-phase CO after 15 min of adsorption. They can be attributed to CO adsorbed on Zr^{3+} and Zr^{4+} cations respectively [27,49]. At higher CO exposure the IR bands at 1632 and 1413 cm^{-1} are also observed, corresponding to formate and hydrogen-carbonate species due to the interaction of adsorbed CO with Zr−OH [27]. In Fig. 5b and c for the pc-Ni/t-ZrO_2 and pfc-Ni/t-ZrO_2 samples CO/Zr-ions peaks vanish completely, which implies that the density of coordinatively unsaturated Zr ions sites is higher on the iwi-Ni/m-ZrO_2 sample than the samples prepared by co-precipitation, since CO is known to be adsorbed at coordinatively unsaturated Zr ions with oxygen vacancies. The CO adsorption on Ni metal supported on t-ZrO_2, corresponding to the peaks at 2082 and 1922 cm^{-1}, is found to be much weaker than that on m-ZrO_2. They are so weak that the bridge-bonded CO peaks totally disappear along with the removal of gas-phase CO, implying its low adsorption strength. On the contrary, the CO/Ni bands remain on the iwi-Ni/m-ZrO_2 spectrum during CO desorption when the CO/Zr-ions bands totally disappear. Moreover, a blue-shift of the band at 1912 cm^{-1} over iwi-Ni/m-ZrO_2 catalyst to 1922 cm^{-1} over pc-Ni/t-ZrO_2 and to 1947 cm^{-1} over pfc-Ni/t-ZrO_2 is observed. These two facts mean the higher electron density of Ni on m-ZrO_2: iwi-Ni/m-ZrO_2 > pc-Ni/t-ZrO_2 > pfc-Ni/t-ZrO_2 as confirmed by the XPS results above.

3.2. DFT calculations

The effect of pristine and oxygen-deficient ZrO_2 supports on the adsorption and electronic structure of Ni clusters was investigated by means of density functional theory.

Two model systems of Ni supported on ZrO_2 was studied, including (i) Ni_4 cluster supported on pristine ZrO_2 surface via Ni−O−Zr bonding (Fig. 6a) and (ii) Ni_4 cluster directly connected to the same ZrO_2 surface with an oxygen vacancy (Fig. 6b). It is found that the stability of Ni_4 clusters had been enhanced greatly in System (ii), in which the adsorption energy changes from −4.15 eV on pristine ZrO_2 to −6.43 eV on O-deficient ZrO_2. Especially, the electronic property of Ni changes on the two kinds of ZrO_2. On pristine ZrO_2 surface in System (i) all the Ni atoms carry extra positive charge ranging from 0.09 to 0.17 eV (Fig. 6a), which is consistent with the literature [14,50] that through strong metal support interaction via Ni-O-M bond (M is the metal of support) electron transfers from Ni to the support so that nickel metal becomes positively charged. Fig. 6c shows the charge distribution on the catalyst system (i) where the positive charge is seen on Ni clusters while there is negative charge on Zr atoms. In the catalyst system (ii) with the removal of the O atom bridging the Ni atom and Zr atom, the Ni atom becomes negatively charged to −0.22 eV (Fig. 6b), indicating the electron initially trapped in the oxygen vacancy being partially transferred to the Ni atom. This results in an increased electron density at the interface between the Ni cluster and the ZrO_2 support as shown in Fig. 6d. In short the DFT calculation illustrates that the negative charge accumulated on Ni clusters stems from the electrons trapped in the oxygen vacancies whereas positive charge accumulation

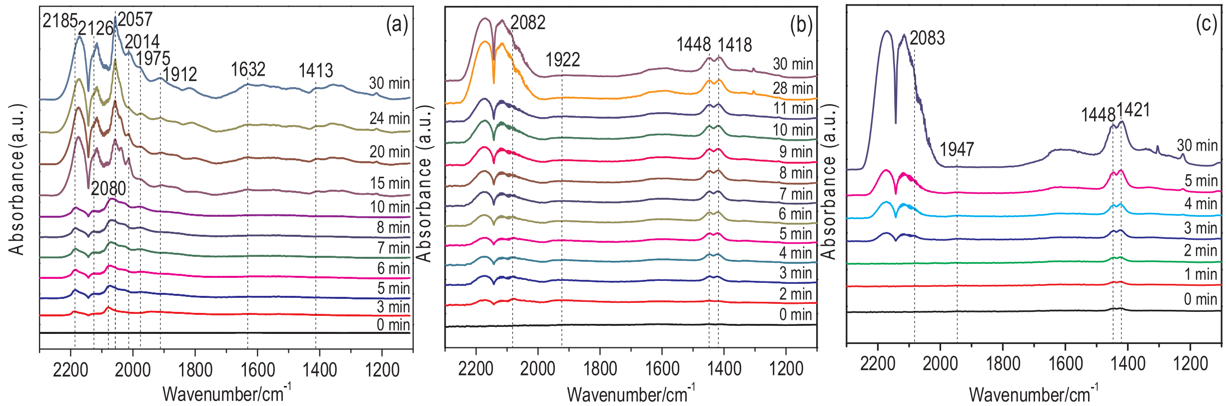

Fig. 5. In situ FTIR spectra of CO adsorption on the reduced Ni/ZrO_2 catalysts: (a) iwi-Ni/m-ZrO_2; (b) pc-Ni/t-ZrO_2; (c) pfc-Ni/t-ZrO_2.

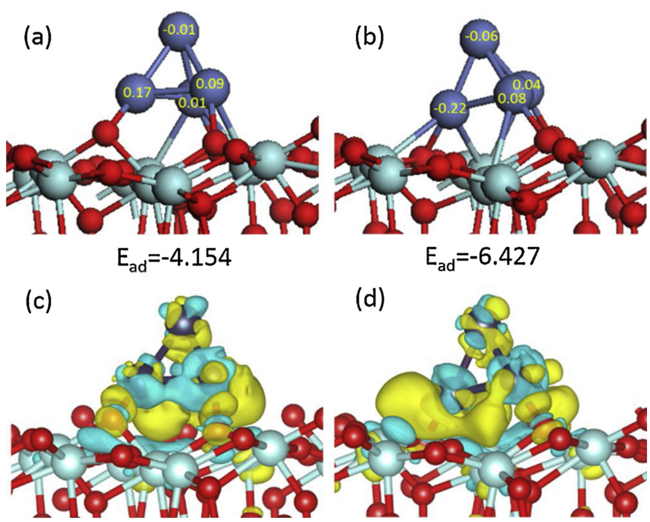

Fig. 6. Structure and electron density of a Ni cluster supported on a ZrO_2 surface: (a) Ni clusters connected to pristine ZrO_2 via an O atom; (b) Ni clusters connected directly to oxygen-deficient ZrO_2; (c) Electron density distribution of (a); (d) Electron density distribution of (b). Blue, Ni; Red, O; Light blue, Zr; Yellow, negative charge; Turquoise, positive charge (For interpretation of the references to colour in this figure legend, the reader is referred to the web version of this article).

on Ni cluster stems from the electron transfer to the support via Ni – O – Zr bond.

3.3. Catalytic performance of the Ni/ZrO_2 catalysts

The catalytic performance of the Ni/ZrO_2 catalysts is displayed in Table 2 and Fig. S2. Under the reaction conditions stated in Table 2, stearic acid $C_{17}H_{35}COOH$ can be converted to n-heptadecane (HD) n-$C_{17}H_{36}$ via hydrodeoxygenation to C_{18} aldehyde, followed by hydrodecarbonylation [that is $C_{17}H_{35}COOH \rightarrow C_{17}H_{35}CHO \rightarrow C_{17}H_{36}$], or to 1-octadecanol (ODL) $C_{18}H_{35}OH$ via hydrodeoxygenation and hydrogenation [that is $C_{17}H_{35}COOH \rightarrow C_{17}H_{35}CHO \rightarrow C_{18}H_{35}OH$]. Other gaseous byproducts (via cracking) such as CH_4, CO and CO_2 can also be detected. Comparing the catalytic selectivity of the three Ni/ZrO_2 catalysts at low conversion levels (< 10%), the iwi-Ni/m-ZrO_2 catalyst (entry 1) showed very high selectivity to 1-octadecanol (S_{ODL} = 93.5%) and the lowest selectivity to n-heptadecane (S_{HD} = 3.16%), while the pfc-Ni/t-ZrO_2 catalyst (entry 3) showed the highest S_{HD} (57.18%) and the lowest S_{ODL} (36.89%). The selectivity to 1-octadecanol follows the same order of electron density of Ni: iwi-Ni/m-ZrO_2 > pc-Ni/t-ZrO_2 > pfc-Ni/t-ZrO_2, while the selectivity to n-heptadecane follows the reverse trend. This implies that the catalytic selectivity of Ni/ZrO_2 catalysts is directly correlated to the electron density of Ni metals.

Table 2
Catalytic performance of the Ni/ZrO_2 catalysts[a].

Entry	Catalysts	t (h)	Conversion (%)	Selectivity (%)[b]			
				n-C_{17}	n-C_{18}	A	C
1	iwi-Ni/m-ZrO_2	1.0	7.47	3.16	0.81	93.5	2.53
2	pc-Ni/t-ZrO_2	1.0	6.15	54.31	3.32	40.03	2.34
3	pfc-Ni/t-ZiO_2	1.0	5.95	57.18	3.75	36.89	2.18
4	iwi-Ni/m-ZrO_2	37	93.77	64.55	7.11	26.51	1.83
5	pc-Ni/t-ZrO_2	36	99.91	86.67	5.72	6.13	1.48
6	pfc-Ni/t-ZiO_2	36	99.89	86.03	6.0	6.47	1.50

[a] Reaction conditions: stearic acid (1.0 g), n-heptane (100 ml), catalyst (0.036 g), 513 K, 4 MPa.
[b] n-C_{17} = n-heptadecane, n-C_{18} = n-octadecane, A = 1-octadecanol, C = cracking products.

With the reaction progressing, the adsorption of formed oxygenates (C_{18} aldehyde and/or 1-octadecanol) on the ZrO_2 support supplemented the oxygen vacancies [4,5], and thus the electron density of Ni metals descended. As a result, the S_{ODL} gradually decreased and reached 26.51% at higher conversion (93.77%) over iwi-Ni/m-ZrO_2 catalyst (entry 4), whereas the S_{HD} increased to 64.55%. A similar selectivity behavior could be also observed over pc-Ni/t-ZrO_2 (entry 5) and pfc-Ni/t-ZrO_2 (entry 6). However, this decline in the S_{ODL} could be alleviated by the presence of more hydrogen which restored the oxygen vacancies. As shown in Fig. S3, the S_{ODL} could be as high as 62.91% at near complete conversion (98.33%) when the reaction was carried out at 5 MPa of H_2. To the best of our knowledge, this is the highest yield of 1-octadecanol (61.86%) reported so far for additive-free monometallic Ni catalysts.

3.4. Reaction mechanism

In order to be able to unequivocally attribute the different selectivities (Table 2) to the electronic effect of Ni/ZrO_2 catalysts, two physicochemical factors influencing the selectivity of catalysts must be excluded, one being the metal particle size effect, and another being the support acidity. First of all, the particle size of Ni metals for the three Ni/ZrO_2 catalysts is comparable, the difference of which is less than 0.7 nm (Table 1). To completely eliminate the particle size effect we carried out experiments over a series of iwi-Ni/m-ZrO_2 catalysts with different Ni loadings (2 wt.%, 5 wt.% and 10 wt.%), in which the particle size of Ni metals varied from 2.5 nm, 5.2 nm to 7.0 nm (Fig. S4). As shown in Fig. S5, the results corroborate that there was essentially no difference in selectivities over these catalysts, neither S_{ODL} nor S_{HD}, indicating there is no correlation between the selectivity and the particle size of Ni metals. The absence of structure-sensitive effect for the

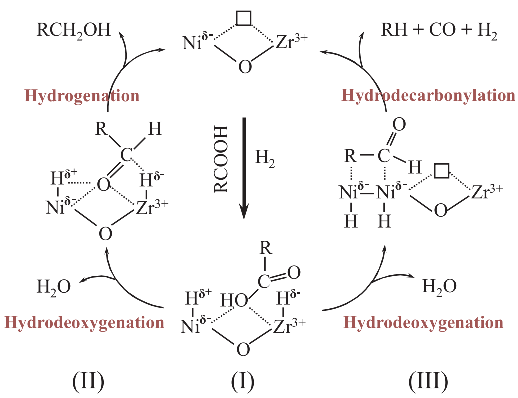

Scheme 1. A proposed mechanism of hydrogenation of fatty acids on the Ni/ZrO_2 catalysts.

hydrogenation of stearic acid was also demonstrated in the literature [6]. Second, the support acidity might have an effect on the catalytic performance [13,51], thus the acidity and basicity of the three Ni catalysts were determined by NH_3-TPD and CO_2-TPD, respectively, and shown in Table S1. A similar distribution and concentration of acid and basic sites were measured, indicating the effect of support acidity can be minimized.

Then, we are allowed to propose a synergistic Ni and ZrO_2 catalyzed reaction mechanism, based on the above characterization and catalytic test results. As shown in Scheme 1(I), the active center consists of metallic Ni and ZrO_2 at its perimeter. There exist oxygen vacancies (O_V) on the ZrO_2 surfaces, which can be supplemented by oxygen atoms in carboxylic or carbonyl groups. Our DFT calculation reveals that the interfacial Ni sites adjacent to oxygen vacancy carry out partially negative charge while Zr ions carry partially positive charge. Hence the active center is denoted as $Ni^{\delta-}$-O_V-Zr^{3+}. During the reaction heterolysis of H_2 is expected to generate $H^{\delta+}$ at Ni sites and $H^{\delta-}$ at Zr-ion sites [40], as observed in H_2-TPD profiles. Meanwhile stearic acid RCOOH can be adsorbed at the oxygen vacancies via its carboxylate group.

The synergetic Ni and ZrO_2 catalyzed hydrodeoxygenation of RCOOH (to aldehyde RCHO) is proposed to proceed by two concerted steps: one involving the attach of $H^{\delta+}$ from Ni site, which removes the carboxylate −OH group as water and form acyl intermediate [52], and the other involving the addition of $H^{\delta-}$ from the Zr-ion site. As shown in Scheme 1, the intermediate aldehyde on the active center can be converted to different products via two parallel pathways: either via hydrogenation of aldehyde C=O to produce alcohol RCH_2OH (Scheme 1(II)), or via hydrodecarbonylation to produce alkane RH (Scheme 1(III)). As shown in XPS spectra, excess electron density of metal Ni is highest on the iwi-Ni/m-ZrO_2 among three Ni/ZrO_2 catalysts, which leads to the higher capability of the $Ni^{\delta-}$-O_V-Zr^{3+} active sites for the heterolysis of H_2 as reported in the literature [41,42,53]. Thus the higher selectivity (93.5%) to 1-octadecanol RCH_2OH (via the hydrogenation of aldehyde RCHO) of the iwi-Ni/m-ZrO_2 catalyst than that of pc-Ni/t-ZrO_2 (40.03%) or pfc-Ni/t-ZrO_2 (36.89%) catalysts can be attributed to the highest density of the $H^{\delta+}$-$Ni^{\delta-}$-O_V-Zr^{3+}-$H^{\delta-}$ active species on the iwi-Ni/m-ZrO_2 catalyst. In contrast, the conversion of the aldehyde intermediate RHCO on pfc-Ni/t-ZrO_2 proceeds mainly via cleavage of C−CHO (decarbonylation). Since the C−C scission needs H atoms [53], the high selectivity (57.18%) to alkane n-C_{17} measured for the pfc-Ni/t-ZrO_2 catalyst is related to the high capability of Ni active sites for the homolytic cleavage of H_2 (see Scheme 1(III)). This is consistent with the electron density of Ni, i.e. pfc-Ni/t-ZrO_2 < pc-Ni/t-ZrO_2 < iwi-Ni/m-ZrO_2.

Therefore, we propose that for the iwi-Ni/m-ZrO_2 catalyst the $Ni^{\delta-}$-O_V-Zr^{3+} active sites are responsible for the heterolysis of H_2 to form $H^{\delta+}$-$Ni^{\delta-}$-O_V-Zr^{3+}-$H^{\delta-}$ species. These species are active for both hydrodeoxygenation of RCOOH to aldehyde RCHO and subsequent hydrogenation of aldehyde to produce alcohol RCH_2OH. For pc-Ni/t-ZrO_2 or pfc-Ni/t-ZrO_2 catalysts, the capability of $Ni^{\delta-}$-O_V-Zr^{3+} sites for the heterolytic cleavage of H_2 is lower than that of the iwi-Ni/m-ZrO_2 catalyst, as shown in H_2-TPD (lack of the 887 K peak) and XPS spectra (higher binding energy of Ni 2p). They are not only able to catalyze the hydrodeoxygenation of RCOOH to aldehyde RCHO but also active for homolysis of H_2 for the C−C scission to produce alkane RH. This explains the high selectivity to n-heptadecane over t-ZrO_2 supported catalysts.

3.5. Discussion

In this contribution, three Ni/ZrO_2 catalysts were synthesized through incipient-wetness impregnation (iwi), positive co-precipitation (pc) and parallel flow co-precipitation (pfc) methods. The resultant catalysts have two ZrO_2 crystal phases, namely monoclinic phase and tetragonal phase. The presence of tetragonal phase in catalysts prepared by co-precipitation methods indicates that the incorporation of Ni^{2+} ions in the lattice of ZrO_2 can stabilize the tetragonal phase by compensating for the negative charge of oxygen vacancies [25]. This implies the interaction of NiO with ZrO_2 in pc- and pfc-Ni/t-ZrO_2 catalysts should be stronger than that in the iwi-Ni/m-ZrO_2 catalyst. As a proof, the reduction temperature of NiO particles in the three catalysts follows the order: iwi-Ni/m-ZrO_2 < pc-Ni/t-ZrO_2 < pfc-Ni/t-ZrO_2, as shown in H_2-TPR (Fig. S1). During the reduction, hydrogen which is dissociatively adsorbed on the Ni metals may spillover to the ZrO_2 support, reacting with Zr−OH and forming water that then desorbs from the surface with the formation of more oxygen vacancies. This requires more Ni^{2+} ions to compensate for the newly formed oxygen vacancies in pc- and pfc-Ni/t-ZrO_2 catalysts, whereas no such requirement is need for iwi-Ni/m-ZrO_2, thus lower reducibility is measured over the catalysts prepared by co-precipitation methods (Table 1).

After the reduction, the crystallinity of the tetragonal phase of pc- and pfc-Ni/t-ZrO_2 catalysts becomes better (Fig. 1(B)), suggesting the formation of more oxygen vacancies and more Ni^{2+} ions are utilized for catalyst stabilization. However, the electrons trapped in the oxygen vacancies are stabilized and localized, and the possibility of electron transfer to Ni metals at interface is limited. XPS results give us the same picture about this metal-support interaction (Fig. 4). Besides the higher intensity at ~854 eV corresponding to more Ni^{2+} ions on pc- and pfc-Ni/t-ZrO_2 catalysts, the less electron-rich of metal Ni (~852.1 eV) than that (851.6 eV) on the iwi-Ni/m-ZrO_2 catalyst corroborates the fact that the electrons in the oxygen vacancies of pc- and pfc-Ni/t-ZrO_2 catalysts are less active and mobile. Since the Ni 2p BE values for pc- and pfc-Ni/t-ZrO_2 catalysts are lower than that of bulk metal Ni (852.7 eV), some limited electron transfer may occur and generate a finite number of $Ni^{\delta-}$-O_V-Zr^{3+} sites.

This electron transfer is significantly facilitated on the iwi-Ni/m-ZrO_2 catalyst due to the presence of more oxygen vacancies evidenced by calculating the atomic ratio of O_I/Zr in XPS spectra, as a result more $Ni^{\delta-}$-O_V-Zr^{3+} sites are produced and also reflected in the in situ FTIR spectra of CO adsorption. The electron-enrichment of metal Ni ($Ni^{\delta-}$) renders the catalyst favorable for heterolysis of H_2, and the H anions ($H^{\delta-}$) generated can be stabilized by the Zr^{3+} ions (as shown the 887 K peak in H_2-TPD), forming $H^{\delta+}$-$Ni^{\delta-}$-O_V-Zr^{3+}-$H^{\delta-}$ species for subsequent hydrogenation reactions.

As illustrated in Scheme 1, these $H^{\delta+}$-$Ni^{\delta-}$-O_V-Zr^{3+}-$H^{\delta-}$ species are active in the hydrodeoxygenation of fatty acid RCOOH to aldehyde RCHO (the rate-determine step) [8]. To shed light on the role of these active species, we calculated the TOFs of the three studied catalysts and attempted to compare with other catalytic systems reported in the literature (Table S2). The TOF value of the iwi-Ni/m-ZrO_2 catalyst is about 9 times than those of pc- and pfc-Ni/t-ZrO_2 catalysts (entries 1–3 in Table S2), suggesting higher amount of these species on the iwi-Ni/m-ZrO_2 catalyst, in good agreement with our characterization results. As for the selectivity of the three catalysts, the alcohol RCH_2OH

produced by subsequent hydrogenation of aldehyde is considered in equilibrium with the aldehyde, the fast hydrogenation of aldehyde will shift the equilibrium towards alcohol. It is known H anions are very active species towards the hydrogenation of polarized C=O band [54], and the iwi-Ni/m-ZrO_2 catalyst possesses the highest amount of H anions in the form of $H^{\delta+}$-$Ni^{\delta-}$-O_V-Zr^{3+}-$H^{\delta-}$ species, thus the equilibrium is shifted towards the alcohol on the iwi-Ni/m-ZrO_2 catalyst. On the other hand, the decarbonylation of aldehyde (via C−C band cleavage) is suppressed, because it requires the presence of H atoms generated on electroneutral Ni metal. Under this circumstance, the hydrogenation of RCOOH to alcohol is greatly promoted, while the decarbonylation of aldehyde is suppressed on the iwi-Ni/m-ZrO_2 catalyst. On the contrary, the decarbonylation of aldehyde more likely occur over pc- and pfc-Ni/t-ZrO_2 catalysts where Ni metal is more electroneutral. Moreover, it was reported that Ni^{2+} ions are active for decarbonylation [10], considering our pc- and pfc-Ni/t-ZrO_2 catalysts have approximately 4 wt.% Ni^{2+} ions (calculated from the reducibility in Table 1), the possibility for decarbonylation is higher than that on the iwi-Ni/m-ZrO_2 catalyst. Therefore, the selectivity towards alcohol is much higher on the iwi-Ni/m-ZrO_2 catalyst (93.5%) than on pc-Ni/t-ZrO_2 (40.03%) and pfc-Ni/t-ZrO_2 (36.89%) catalysts.

Comparing the TOFs of our catalysts with other catalysts reported (Table S2), it seems that no correlation between the selectivity with TOFs can be observed, neither on Ni-based (Fig. S6) nor noble-metal-based catalysts (Fig. S7). This is because physicochemical properties of catalysts (especially acidity and basicity), catalyst preparation methods, and reaction conditions all have influence on the selectivity of catalysts [8]. The catalytic performance should be compared after considering all these influential factors before any conclusion is made. In this work, the metal particle size effect and the support acidity and basicity effects are excluded, which allows us to compare the three Ni/ZrO_2 catalysts under identical reaction conditions and attribute unequivocally the different selectivities to the electronic effect of catalysts.

During the prolonged reaction, the oxygen vacancies on the ZrO_2 support are gradually supplemented by the adsorption of formed oxygenates (C_{18} aldehyde and/or 1-octadecanol). Fortunately, the consumption of oxygen vacancies can be alleviated by the presence of excess H_2, for instance 5 MPa H_2, and up to 62.91% S_{ODL} at near complete conversion (98.33%) can be obtained. This leads to the yield of 1-octadecanol (61.86%) which is the highest reported so far for additive-free monometallic Ni catalysts. From the environmental and economic point of views, this contribution not only addresses the environmental concerns regarding the use of commercial Cu-Cr catalysts, but also reduces the operation cost by utilizing lower reaction temperature and hydrogen pressure (240 °C and 4 MPa) than those (250–350 °C and 10–20 MPa) for fatty alcohol production [55,56].

4. Conclusions

Three Ni/ZrO_2 catalysts with various degrees of oxygen deficiency in ZrO_2 support were synthesized, so that the electron density of nickel in the reduced Ni/ZrO_2 catalysts could be tuned, which would lead to different selectivities in hydrogenation of fatty acids (FA) to fuel-like alkanes or fatty alcohols. Charge transfer from the ZrO_2 support to metallic Ni was found to take place on all the three catalysts, depending on the concentration of oxygen defects. The electron density of metal Ni on the iwi-Ni/ZrO_2 sample was higher than that of the t-ZrO_2 supported Ni metals, due to the higher negative charge density accumulated at the oxygen defects on the m-ZrO_2 surface as compared to t-ZrO_2. The Ni sites at the perimeter of oxygen-deficient ZrO_2 ($Ni^{\delta-}$-O_V-Zr^{3+}) are considered to play role as the active center for FA transformation. The negatively charged metal Ni promotes the heterolysis of H_2 and the subsequent hydrogenation of adsorbed FA to aldehyde intermediate. On m-ZrO_2 metallic Ni with higher electron density further catalyzes the hydrogenation of the aldehyde to 1-octadecanol, while on t-ZrO_2 Ni metals with lower excess electron density are in more favor of the C−C bond cleavage (than the hydrogenation of C=O) of the aldehyde intermediate to produce n-heptadecane.

Acknowledgments

The authors acknowledge the financial support from the National Natural Science Foundation of China (NSFC Grant No. 21875220, 21303163), the Zhejiang Provincial Natural Science Foundation of China (LY17B060006, LY19B030007), the Qianjiang Talent Project in Zhejiang Province (QJD1302011) and the Scientific Research Fund of Zhejiang Provincial Education Department (Y201328681).

Appendix A. Supplementary data

Supplementary material related to this article can be found, in the online version, at doi:https://doi.org/10.1016/j.apcatb.2019.04.043.

References

[1] H. Zhang, H. Lin, W. Wang, Y. Zheng, P. Hu, Hydroprocessing of waste cooking oil over a dispersed nano catalyst: kinetics study and temperature effect, Appl. Catal. B: Environ. 150–151 (2014) 238–248.
[2] A.E. Coumans, E.J.M. Hensen, A model compound (methyl oleate, oleic acid, triolein) study of triglycerides hydrodeoxygenation over alumina-supported NiMo sulfide, Appl. Catal. B: Environ. 201 (2017) 290–301.
[3] M. Snåre, I. Kubičková, P. Mäki-Arvela, K. Eränen, D.Y. Murzin, Heterogeneous catalytic deoxygenation of stearic acid for production of biodiesel, Ind. Eng. Chem. Res. 45 (2006) 5708–5715.
[4] B. Peng, X. Yuan, C. Zhao, J.A. Lercher, Stabilizing catalytic pathways via redundancy: selective reduction of microalgae oil to alkanes, J. Am. Chem. Soc. 134 (2012) 9400–9405.
[5] B. Peng, C. Zhao, S. Kasakov, S. Foraita, J.A. Lercher, Manipulating catalytic pathways: deoxygenation of palmitic acid on multifunctional catalysts, Chem. Eur. J. 19 (2013) 4732–4741.
[6] W. Song, C. Zhao, J.A. Lercher, Importance of size and distribution of Ni nanoparticles for the hydrodeoxygenation of microalgae oil, Chem. Eur. J. 19 (2013) 9833–9842.
[7] H. Xin, K. Guo, D. Li, H. Yang, C. Hu, Production of high-grade diesel from palmitic acid over activated carbon-supported nickel phosphide catalysts, Appl. Catal. B: Environ. 187 (2016) 375–385.
[8] C. Kordulis, K. Bourikas, M. Gousi, E. Kordouli, A. Lycourghiotis, Development of nickel based catalysts for the transformation of natural triglycerides and related compounds into green diesel: a critical review, Appl. Catal. B: Environ. 181 (2016) 156–196.
[9] E. Kordouli, L. Sygellou, C. Kordulis, K. Bourikas, A. Lycourghiotis, Probing the synergistic ratio of the NiMo/γ-Al_2O_3 reduced catalysts for the transformation of natural triglycerides into green diesel, Appl. Catal. B: Environ. 209 (2017) 12–22.
[10] E. Kordouli, B. Pawelec, K. Bourikas, C. Kordulis, J.L.G. Fierro, A. Lycourghiotis, Mo promoted Ni-Al_2O_3 co-precipitated catalysts for green diesel production, Appl. Catal. B: Environ. 229 (2018) 139–154.
[11] C. Zhao, T. Brück, J.A. Lercher, Catalytic deoxygenation of microalgae oil to green hydrocarbons, Green Chem. 15 (2013) 1720–1739.
[12] R. Loe, E. Santillan-Jimenez, T. Morgan, L. Sewell, Y. Ji, S. Jones, M.A. Isaacs, A.F. Lee, M. Crocker, Effect of Cu and Sn promotion on the catalytic deoxygenation of model and algal lipids to fuel-like hydrocarbons over supported Ni catalysts, Appl. Catal. B: Environ. 191 (2016) 147–156.
[13] I. Hachemi, N. Kumar, P. Mäki-Arvela, J. Roine, M. Peurla, J. Hemming, J. Salonen, D.Y. Murzin, Sulfur-free Ni catalyst for production of green diesel by hydrodeoxygenation, J. Catal. 347 (2017) 205–221.
[14] B. Wang, Y. Xiong, Y. Han, J. Hong, Y. Zhang, J. Li, F. Jing, W. Chu, Preparation of stable and highly active Ni/CeO_2 catalysts by glow discharge plasma technique for glycerol steam reforming, Appl. Catal. B: Environ. 249 (2019) 257–265.
[15] W. Yang, X. Yang, J. Jia, C. Hou, H. Gao, Y. Mao, C. Wang, J. Lin, X. Luo, Oxygen vacancies confined in ultrathin nickel oxide nanosheets for enhanced electrocatalytic methanol oxidation, Appl. Catal. B: Environ. 244 (2019) 1096–1102.
[16] J. Ren, H. Li, Y. Jin, J. Zhu, S. Liu, J. Lin, Z. Li, Silica/titania composite-supported Ni catalysts for CO methanation: effects of Ti species on the activity, anti-sintering, and anti-coking properties, Appl. Catal. B: Environ. 201 (2017) 561–572.
[17] A.M. Abdel-Mageed, D. Widmann, S.E. Olesen, I. Chorkendorff, J. Biskupek, R.J. Behm, Selective CO methanation on Ru/TiO_2 catalysts: role and influence of metal-support interactions, ACS Catal. 5 (2015) 6753–6763.
[18] F. Liao, Y. Huang, J. Ge, W. Zheng, K. Tedsree, P. Collier, X. Hong, S.C. Tsang, Morphology-dependent interactions of ZnO with Cu nanoparticles at the materials' interface in selective hydrogenation of CO_2 to CH_3OH, Angew. Chem. Int. Ed. 50 (2011) 2162–2165.
[19] F. Liao, Z. Zeng, C. Eley, Q. Lu, X. Hong, S.C.E. Tsang, Electronic modulation of a copper/zinc oxide catalyst by a heterojunction for selective hydrogenation of carbon dioxide to methanol, Angew. Chem. Int. Ed. 51 (2012) 5832–5836.
[20] X. Zhou, J. Qu, F. Xu, J. Hu, J.S. Foord, Z. Zeng, X. Hong, S.C. Edman Tsang, Shape selective plate-form Ga_2O_3 with strong metal-support interaction to overlying Pd for

hydrogenation of $CO_2$to CH_3OH, Chem. Commun. 49 (2013) 1747–1749.
[21] N. Claudine, Polar oxide surfaces, J. Phys. Condens. Matter 12 (2000) R367–R410.
[22] G. Jacek, F. Fabio, N. Claudine, Polarity of oxide surfaces and nanostructures, Rep. Prog. Phys. 71 (2008) 016501.
[23] M.V. Ganduglia-Pirovano, A. Hofmann, J. Sauer, Oxygen vacancies in transition metal and rare earth oxides: current state of understanding and remaining challenges, Surf. Sci. Rep. 62 (2007) 219–270.
[24] M. Zhang, J. Zhang, Y. Wu, J. Pan, Q. Zhang, Y. Tan, Y. Han, Insight into the effects of the oxygen species over Ni/ZrO_2 catalyst surface on methane reforming with carbon dioxide, Appl. Catal. B: Environ. 244 (2019) 427–437.
[25] K. Samson, M. Śliwa, R.P. Socha, K. Góra-Marek, D. Mucha, D. Rutkowska-Zbik, J.F. Paul, M. Ruggiero-Mikołajczyk, R. Grabowski, J. Słoczyński, Influence of ZrO_2 structure and copper electronic state on activity of Cu/ZrO_2 catalysts in methanol synthesis from CO_2, ACS Catal. 4 (2014) 3730–3741.
[26] K. Pokrovski, K.T. Jung, A.T. Bell, Investigation of CO and CO_2 adsorption on tetragonal and monoclinic zirconia, Langmuir 17 (2001) 4297–4303.
[27] S. Kouva, K. Honkala, L. Lefferts, J. Kanervo, Review: monoclinic zirconia, its surface sites and their interaction with carbon monoxide, Catal. Sci. Technol. 5 (2015) 3473–3490.
[28] C.H. Bartholomew, R.B. Pannell, The stoichiometry of hydrogen and carbon monoxide chemisorption on alumina- and silica-supported nickel, J. Catal. 65 (1980) 390–401.
[29] D.G. Mustard, C.H. Bartholomew, Determination of metal crystallite size and morphology in supported nickel catalysts, J. Catal. 67 (1981) 186–206.
[30] J.P. Perdew, J.A. Chevary, S.H. Vosko, K.A. Jackson, M.R. Pederson, D.J. Singh, C. Fiolhais, Atoms, molecules, solids, and surfaces: applications of the generalized gradient approximation for exchange and correlation, Phys. Rev. B 46 (1992) 6671–6687.
[31] G. Kresse, J. Hafner, Ab initio molecular dynamics for liquid metals, Phys. Rev. B 47 (1993) 558–561.
[32] G. Kresse, J. Hafner, Norm-conserving and ultrasoft pseudopotentials for first-row and transition elements, J. Phys.: Condens. Matter 6 (1994) 8245–8257.
[33] G. Kresse, J. Furthmüller, Efficient iterative schemes for ab initio total-energy calculations using a plane-wave basis set, Phys. Rev. B 54 (1996) 11169–11186.
[34] J.P. Perdew, Y. Wang, Accurate and simple analytic representation of the electron-gas correlation energy, Phys. Rev. B 45 (1992) 13244–13249.
[35] R. Ruh, T.J. Rockett, Proposed phase diagram for the system ZrO_2, J. Am. Ceram. Soc. 53 (1970) 360-360.
[36] L.K. Dash, N. Vast, P. Baranek, M.-C. Cheynet, L. Reining, Electronic structure and electron energy-loss spectroscopy of ZrO_2 zirconia, Phys. Rev. B 70 (2004) 245116–245132.
[37] K. Jung, A. Bell, Effects of zirconia phase on the synthesis of methanol over zirconia-supported copper, Catal. Lett. 80 (2002) 63–68.
[38] M.D. Rhodes, A.T. Bell, The effects of zirconia morphology on methanol synthesis from CO and over catalysts: part I. Steady-state studies, J. Catal. 233 (2005) 198–209.
[39] I. Heo, D.Y. Yoon, B.K. Cho, I.-S. Nam, J.W. Choung, S. Yoo, Activity and thermal stability of Rh-based catalytic system for an advanced modern TWC, Appl. Catal. B: Environ. 121–122 (2012) 75–87.
[40] A. Trunschke, D.L. Hoang, H. Lieske, In situ FTIR studies of high-temperature adsorption of hydrogen on zirconia, J. Chem. Soc. Faraday Trans. 91 (1995) 4441–4444.
[41] A.G. Sato, D.P. Volanti, D.M. Meira, S. Damyanova, E. Longo, J.M.C. Bueno, Effect of the ZrO_2 phase on the structure and behavior of supported Cu catalysts for ethanol conversion, J. Catal. 307 (2013) 1–17.
[42] H.-Y.T. Chen, S. Tosoni, G. Pacchioni, Hydrogen adsorption, dissociation, and spillover on Ru_{10} clusters supported on anatase TiO_2 and tetragonal ZrO_2 (101) surfaces, ACS Catal. 5 (2015) 5486–5495.
[43] C. Morant, J.M. Sanz, L. Galán, L. Soriano, F. Rueda, An XPS study of the interaction of oxygen with zirconium, Surf. Sci. 218 (1989) 331–345.
[44] S.A. Steiner, T.F. Baumann, B.C. Bayer, R. Blume, M.A. Worsley, W.J. MoberlyChan, E.L. Shaw, R. Schlögl, A.J. Hart, S. Hofmann, B.L. Wardle, Nanoscale zirconia as a nonmetallic catalyst for graphitization of carbon and growth of single- and multi-wall carbon nanotubes, J. Am. Chem. Soc. 131 (2009) 12144–12154.
[45] X. Jia, X. Zhang, N. Rui, X. Hu, C.-j. Liu, Structural effect of Ni/ZrO_2 catalyst on CO_2 methanation with enhanced activity, Appl. Catal. B: Environ. 244 (2019) 159–169.
[46] J.T. Yates, C.W. Garland, Infrared studies of carbon monoxide chemisorbed on nickel and on mercury-poisoned nickel surfaces, J. Phys. Chem. 65 (1961) 617–624.
[47] C.E. O'Neill, D.J.C. Yates, The effect of the support on the infrared spectra of carbon monoxide adsorbed on nickel, J. Phys. Chem. 65 (1961) 901–906.
[48] M. Mihaylov, K. Hadjiivanov, FTIR study of CO and NO adsorption and coadsorption on Ni-ZSM-5 and Ni/SiO_2, Langmuir 18 (2002) 4376–4383.
[49] P.M. de Souza, R.C. Rabelo-Neto, L.E.P. Borges, G. Jacobs, B.H. Davis, U.M. Graham, D.E. Resasco, F.B. Noronha, Effect of zirconia morphology on hydrodeoxygenation of phenol over Pd/ZrO_2, ACS Catal. 5 (2015) 7385–7398.
[50] L. He, B. Liang, L. Li, X. Yang, Y. Huang, A. Wang, X. Wang, T. Zhang, Cerium-oxide-modified nickel as a non-noble metal catalyst for selective decomposition of hydrous hydrazine to hydrogen, ACS Catal. 5 (2015) 1623–1628.
[51] W. Song, Y. Liu, E. Baráth, C. Zhao, J.A. Lercher, Synergistic effects of Ni and acid sites for hydrogenation and C−O bond cleavage of substituted phenols, Green Chem. 17 (2015) 1204–1218.
[52] L. Di, S. Yao, S. Song, G. Wu, W. Dai, N. Guan, L. Li, Robust ruthenium catalysts for the selective conversion of stearic acid to diesel-range alkanes, Appl. Catal. B: Environ. 201 (2017) 137–149.
[53] R. Prins, Hydrogen spillover. Facts and fiction, Chem. Rev. 112 (2012) 2714–2738.
[54] C. Xu, G. Chen, Y. Zhao, P. Liu, X. Duan, L. Gu, G. Fu, Y. Yuan, N. Zheng, Interfacing with silica boosts the catalysis of copper, Nat. Commun. 9 (2018) 3367.
[55] M.A. Sánchez, G.C. Torres, V.A. Mazzieri, C.L. Pieck, Selective hydrogenation of fatty acids and methyl esters of fatty acids to obtain fatty alcohols-a review, J. Chem. Technol. Biotechnol. 92 (2017) 27–42.
[56] V.O. Rodina, D.Y. Ermakov, A.A. Saraev, S.I. Reshetnikov, V.A. Yakovlev, Influence of reaction conditions and kinetic analysis of the selective hydrogenation of oleic acid toward fatty alcohols on $Ru-Sn-B/Al_2O_3$ in the flow reactor, Appl. Catal. B: Environ. 209 (2017) 611–620.